Histograms should not be used to segment hyperpolarized gas images of the lung

Nicholas J. Tustison, E. Alia, Jaime F. Mata

Department of Radiology and Medical Imaging, University of Virginia, Charlottesville, VA

Corresponding author:
Nicholas J. Tustison, DSc
Department of Radiology and Medical Imaging
University of Virginia
ntustison@virginia.edu

Abstract

Magnetic resonance imaging using hyperpolarized gases has made possible the novel visualization of airspaces, such as the human lung, which has advanced research into the growth, development, and pathologies of the pulmonary system. In conjunction with the innovations associated with image acquisition, multiple image analysis strategies have been proposed and refined for the quantification of such lung imaging with much research effort devoted to semantic segmentation, or voxelwise classification, into clinically-oriented categories based on ventilation levels. Given the functional aspect of these images and the consequent sophistication of the segmentation task, many of these algorithmic approaches reduce the complex spatial image intensity information to intensity-only considerations, which can be contextualized in terms of the intensity histogram. Although facilitating computational processing, this simplifying transformation results in the loss of important spatial cues for identifying salient image features, such as ventilation defects (a well-studied correlate of lung pathophysiology), as spatial objects. In this work, we discuss the interrelatedness of the most common approaches for histogram-based segmentation of hyperpolarized gas lung imaging and evaluate the underlying assumptions associated with each approach demonstrating how these assumptions lead to suboptimal performance, particularly in terms of precision. We then illustrate how a convolutional neural network can be trained to leverage multi-scale spatial information which circumvents the problematic issues associated with these approaches. Importantly, we provide the entire processing and evaluation framework, including the newly reported deep learning functionality, as open-source through the well-known Advanced Normalization Tools ecosystem (ANTsX).

Notes to self:

- Calling CNN “el Bicho” until we can come up a different name.
- Jaime to edit Subsections 2.1?
- Possible co-authors: Tally Altes, Kun Qing, John Mugler, Wilson Miller, James Gee, Mu He
- ~~Need five more young healthy subjects.~~
- Need to finalize experiments
  - Nonlinear experiments: Noise, MR intensity nonlinear mapping, Noise + Nonlinear mapping
  - one issue is “should we preprocess with N4?” — yes, it helps segmentation, and more than one group uses it.

1 Introduction

1.1 Early acquisition and development

Early hyperpolarized gas pulmonary imaging research reported findings in qualitative terms.

Descriptions:

- "^{3}He MRI depicts anatomical structures reliably" (1)
- "hypointense areas" (2)
- "signal intensity inhomogeneities" (2)
- "wedge-shaped areas with less signal intensity" (2)
- "patchy or wedge-shaped defects" (3)
- "ventilation defects" (4)
- "defects were pleural-based, frequently wedge-shaped, and varied in size from tiny to segmental" (4)

1.2 Historical overview of quantification

Early attempts at quantification of ventilation images were limited to enumerating the number of ventilation defects or estimating the proportion of ventilated lung (4–6). This early work has evolved to current techniques which can be generally categorized in order of increasing algorithmic sophistication as follows:

- binary thresholding based on relative intensities (7, 8),
- linear intensity standardization based on global rescaling of the intensity histogram to a reference distribution based on healthy controls, i.e., "linear binning" (9, 10),
- nonlinear intensity standardization based on piecewise affine transformation of the intensity histogram using a customized hierarchical k-means algorithm (11, 12), and

- Gaussian mixture modeling (GMM) of the intensity histogram with Markov random field (MRF) spatial prior modeling (13)

where each of these algorithms has been contextualized in terms of the intensity histogram for facilitating comparison.

An early semi-automated technique used to compare smokers and never-smokers relied on manually drawn regions to determine a threshold value based on the mean signal and noise values (7). Related approaches, which use a simple rescaled threshold value to binarize the ventilation image into ventilated/non-ventilated regions (14), continue to find modern application (8). Similar to the histogram-only algorithms (i.e., linear binning and hierarchical k-means, discussed below), these approaches do not take into account the various MRI artefacts such as noise (15, 16) and the intensity inhomogeneity field (17) which prevent hard threshold values from distinguishing tissue types consistent with that of human experts. In addition, to provide a more granular categorization of ventilation for greater compatibility with clinical qualitative assessment, many current techniques have increased the number of voxel classes (i.e., clusters) beyond the binary categories of "ventilated" and "non-ventilated."

Linear binning is a simplified type of MR intensity standardization (18) in which a set of healthy controls, all intensity normalized to [0, 1], is used to calculate the cluster threshold values, based on an aggregated estimate of the parameters of a single Gaussian fit. A subject image to be segmented is then rescaled to this reference histogram (i.e., a global affine 1-D transform). This mapping results in alignment of the cluster boundaries such that corresponding labels are assumed to have the same clinical interpretation. In addition to the previously mentioned issues associated with hard threshold values, such a global transform does not account for MR intensity nonlinearities that have been well-studied (18–22) and are known to cause significant intensity variation even in the same region of the same subject. As stated in (21):

> Intensities of MR images can vary, even in the same protocol and the same sample and using the same scanner. Indeed, they may depend on the acquisition conditions such as room temperature and hygrometry, calibration adjustment,

slice location, B0 intensity, and the receiver gain value. The consequences of intensity variation are greater when different scanners are used.

As we demonstrate in subsequent sections, ignoring these nonlinearities can have significant consequences in the well-studied (and somewhat analogous) area of brain tissue segmentation in T1-weighted MRI (e.g., (23–25)) and we demonstrate its effect in hyperpolarized gas imaging quantification robustness in conjunction with noise considerations. In addition, it is not a given that we have a sufficient understanding of what constitutes a "normal" in the context of mean and standard deviation MR intensity values and whether or not those values can be combined in a linear fashion to constitute a single reference standard. Of more concrete concern, though, is that the requirement for a healthy cohort for determination of algorithmic parameters introduces a non-negligible source of measurement variance, as we will also demonstrate.

Previous attempts at histogram standardization (18, 20) in light of these MR intensity nonlinearities have relied on 1-D piecewise affine mappings between corresponding structural features found within the histograms themselves (i.e., peaks and valleys). For example, structural MRI, such as T1-weighted neuroimaging, utilizes the well-known relative intensities of major tissues types (i.e., cerebrospinal fluid, gray matter, and white matter), which characteristically correspond to visible histogram peaks, as landmarks to determine the nonlinear intensity mapping between images. However, in hyperpolarized gas imaging of the lung, no such characteristic structural features exist, generally speaking, between histograms. This is most likely due to the primarily functional utility (vs. anatomical) nature of these images. The approach used by some groups (11, 26) of employing some variant of the well-known k-means algorithm as a clustering strategy (27) to minimize the within-class variance of its intensities can be viewed as an alternative optimization strategy for determining a nonlinear mapping between histograms for a clinically-based MR intensity standardization. K-means does constitute an algorithmic approach with additional degrees of flexibility and sophistication over linear binning as it employs basic prior knowledge in the form of a generic clustering desideratum for optimizing a type of MR intensity standardization.[1]

[1]The prior knowledge for histogram mapping is the general machine learning heuristic of clustering samples

Histogram-based optimization is used in conjunction with spatial considerations in the approach detailed in (13). Based on a well-established iterative approach originally used for NASA satellite image processing and subsequently appropriated for brain tissue segmentation in T1-weighted MRI (28), a GMM is used to model the intensity clusters of the histogram with class modulation in the form of probabilistic voxelwise label considerations, i.e., MRF modeling, within image neighborhoods (29) using the expectation-maximization (EM) algorithm (30). Initialization for this particular application is in the form of k-means clustering which, itself, is initialized automatically using evenly spaced cluster centers. This has the advantage, in contrast to k-means and the other algorithms outlined, that it does not use hard intensity thresholds for distinguishing class labels which does demonstrates robustness to certain imaging distortions, such as noise. However, as we will demonstrate, this algorithm is also flawed in that it implicitly assumes, incorrectly, that meaningful structure is found, and can be adequately characterized, within the associated image histogram in order to optimize a multi-class labeling which also leads to susceptibility to MR nonlinear intensity variation.

Additionally, many of these segmentation algorithms use N4 bias correction (31), an extension of the nonuniform intensity normalization (N3) algorithm (17), to mitigate MR intensity inhomogeneity artefacts. Interestingly, N3/N4 also iteratively optimizes towards a final solution using information from both the histogram and image domains. Based on the intuition that the bias field acts as a smoothing convolution operation on the original image intensity histogram, N3/N4 optimizes a nonlinear (i.e., deformable) intensity mapping, based on histogram deconvolution. This nonlinear mapping is constrained such that its effects smoothly vary across the image. Additionally, due to the deconvolution operation, this nonlinear mapping sharpens the histogram peaks which presumably correspond to tissue types. While such assumptions are appropriate for the domain in which N3/N4 was developed (i.e., T1-weighted brain tissue segmentation) and while it is assumed that the enforcement of low-frequency modulation of the intensity mapping prevents new image features from being generated, it is not clear what effects N4 parameter choices have on the final segmentation solution, particularly for those algorithms that are limited to intensity-only considerations

based on the minimizing within-class distance while simultaneously maximizing the between-class distance. In the case of k-means, this "distance" is the intensity variance.

and not robust to the aforementioned MR intensity nonlinearities.

1.3 Motivation for current study

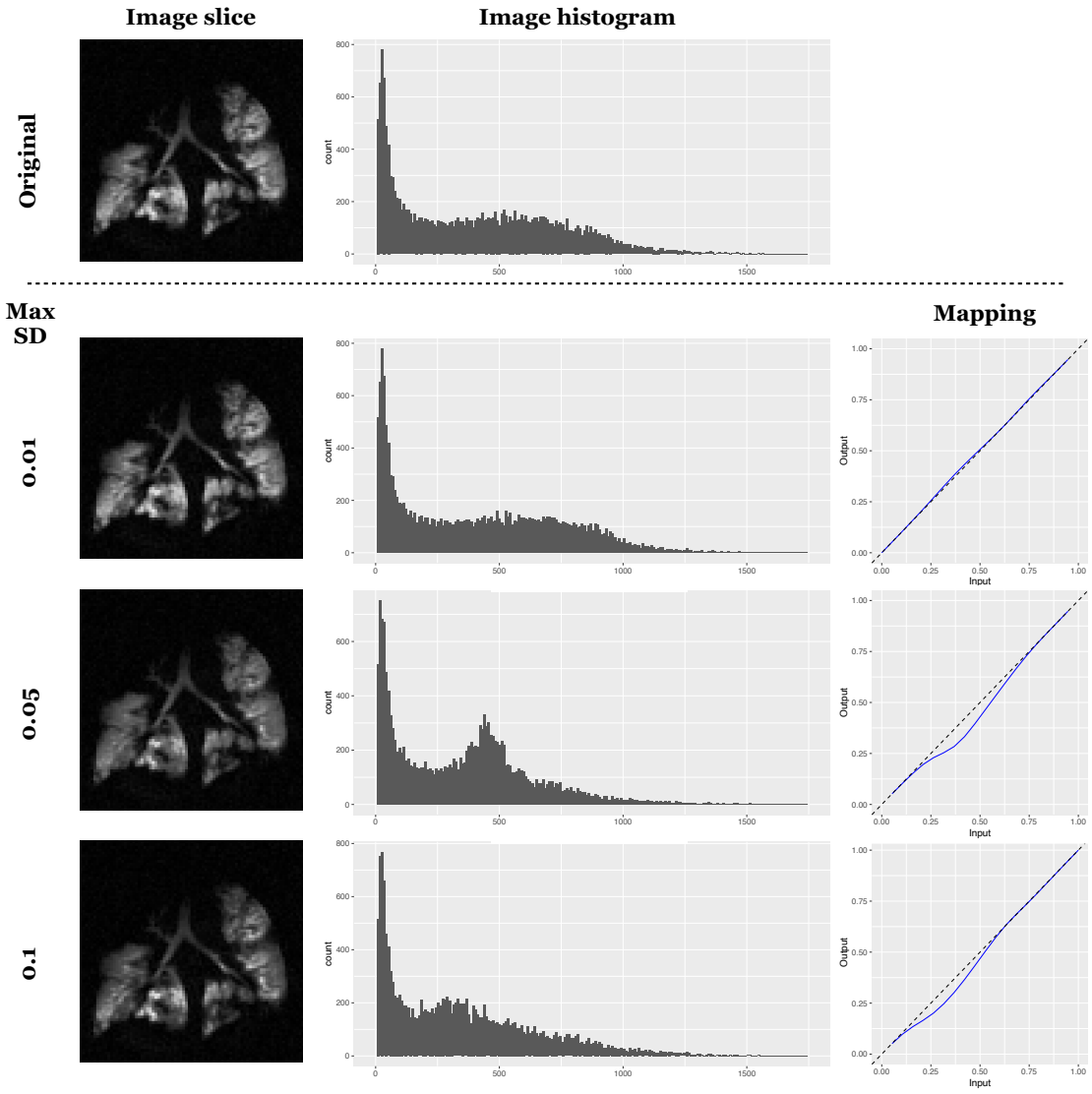

Figure 1: Illustration of the effect of MR nonlinear intensity warping on the histogram structure. We simulate these mappings by perturbing specified points along the bins of the histograms by a Gaussian random variable of 0 mean and specified max standard deviation ("Max SD"). By simulating these types of intensity changes, we can visualize the effects on the underlying intensity histograms and investigate the effects on salient outcome measures. Here we simulate intensity mappings which, although relatively small, can have a significant effect on the histogram structure.

Investigating the assumptions outlined above, particularly those associated with the nonlinear intensity mappings due to both the MR acquisition and inhomogeneity mitigation preprocess-

ing, we became concerned by the susceptibility of the histogram structure to such variations and the potential effects on current clinical measures of interest derived from these algorithms (e.g., ventilation defect percentage). Figure 1 provides a sample visualization representing some of the structural changes that we observed when simulating these nonlinear mappings. It is important to notice that even relatively small alterations in the image intensities can have significant effects on the histogram even though a visual, clinically-based assessment of the image can remain largely unchanged.

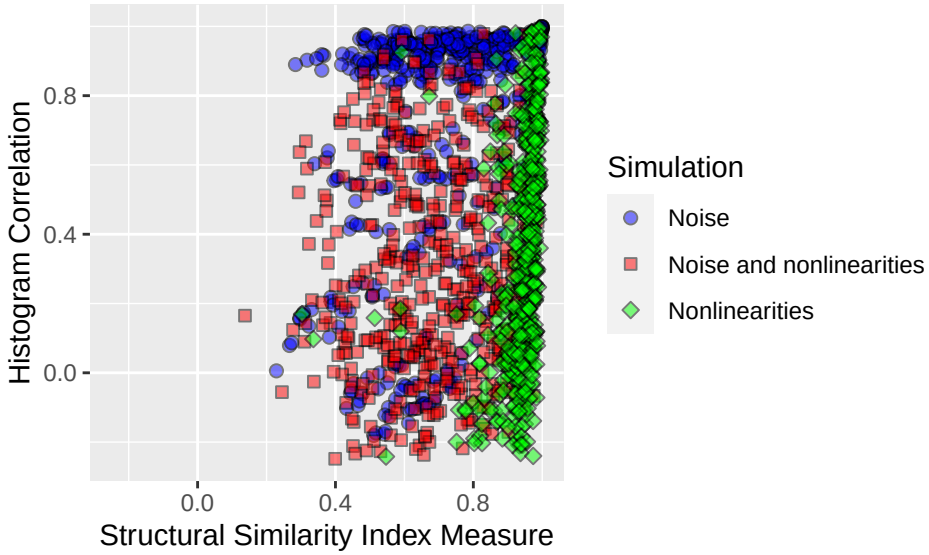

Figure 2: Image-based SSIM vs. histogram-based Pearson's correlation differences under distortions induced by the common MR artefacts of noise and intensity nonlinearities. For the nonlinearity-only simulations, the images maintain their structural integrity as the SSIM values remain close to 1. This is in contrast to the corresponding range in histogram similarity is much larger. Although not as large, the range in histogram differences with simulated noise is much greater than the range in SSIM. Both point to the potential lack of robustness in the histogram domain vs. the image domain in relation to simulated MR artefacts.

To briefly explore these effects further for the purposes of motivating additional experimentation, we provide a summary illustration from a set of image simulations in Figure 2 which are detailed later in this work and used for algorithmic comparison. Simulated MR artefacts were applied to each image which included both noise and nonlinear intensity mappings (and their combination) which made for a total simulated cohort of ~50 images ($\times$10 simulations per image $\times$3 types of artefact simulations). Prior to any algorithmic comparative analysis, we quantified the difference of each simulated image with the corresponding original image using

the structural similarity index measurement (SSIM) (32). SSIM is a highly-cited measure which quantifies structural differences between a reference and distorted (i.e., transformed) image based on known properties of the human visual system. SSIM has a range $[-1, 1]$ where 0 indicates no structural similarity and 1 indicates perfect structural similarity. We also generated the histograms corresponding to these images. Although several histogram similarity measures exist, we chose Pearson's correlation primarily as it resides in the same [min, max] range as SSIM with analogous significance. In addition to the fact that the image-to-histogram transformation discards important spatial information, from Figure 2, it should be apparent that this transformation also results in greater variance in the resulting information under common MR imaging artefacts, according to these measures. Thus, prior to any algorithmic considerations, these observations point to the fact that optimizing in the domain of the histogram will be generally less robust than optimizing directly in the image domain.

Ultimately, we are not claiming that these algorithms are erroneous, per se. Much of the relevant research has been limited to quantifying differences with respect to ventilation versus non-ventilation in various clinical categories and these algorithms have certainly demonstrated the capacity for advancing such research. However, the aforementioned issues influence quantitation in terms of core scientific measurement principles such as precision (e.g., reproducibility and repeatability (33)) and bias which become increasingly significant with multi-site (34) and large-scale studies. In addition, generally speaking, refinements in measuring capabilities correlate with scientific advancement so as acquisition and analysis methodologies improve, so should the level of sophistication and performance of the measurement tools.

In assessing these segmentation algorithms for hyperpolarized gas imaging, it is important to note that human expertise leverages more than relative intensity values to identify salient, clinically relevant features in images—something more akin to the complex neural network structure versus the 1-D intensity histogram. The increased popularity of deep-layered neural networks as (35), particularly convolutional neural networks (CNN), is due to their outstanding performance in certain computational tasks, including classification and semantic segmentation in medical imaging (36). Their potential for leveraging spatial information

from images surpasses the perceptual capabilities of previous approaches and even rivals that of human raters (37). We introduced a deep learning approach in (38) and further expand on that work for comparison with existing approaches in this work. In the spirit of open science, we have made the entire evaluation framework, including our novel contributions, available within our Advanced Normalization Tools software ecosystem (ANTsX) (39).

2 Materials and methods

To support the discussion in the Introduction, we performed various experiments which showcase the effects of both nonlinear intensity mapping and noise artefacts on measurement precision and bias using the popular algorithms described previously, specifically linear binning (9), hierarchical k-means (11), GMM-MRF (specifically, ANTs-based Atropos tailored for functional lung imaging) (13), and a trained CNN (38).

We focus initially on some of the issues unique to linear binning, specifically its susceptibility to MR nonlinearity artefacts as well as the additional requirement of a reference distribution. The latter is motivated qualitatively through the analogous application of T1-weighted brain MR segmentation. This component is strictly qualitative as the visual evidence and previous developmental history within that field should be sufficiently compelling in motivating subsequent quantitative exploration within hyperpolarized gas lung imaging. We use these qualitative results as a segue to quantifying the effects of the choice of reference cohort on the clustering parameters for the linear binning algorithm.

We then incorporate the trained CNN model in exploring additional aspects of measurement variance based on simulating both MR noise and intensity nonlinearities. Finally, we investigate algorithmic accuracy (i.e., bias) in the absence of ground-truth segmentations, by using a clinical diagnostic prediction approach and employing the simultaneous truth and performance level estimation (STAPLE) (40).

2.1 Hyperpolarized gas image cohort

A retrospective dataset was collected consisting of young healthy ($n = 10$), older healthy ($n = 7$), cystic fibrosis (CF) ($n =?$), idiopathic lung disease (ILD) ($n =?$), and chronic obstructive pulmonary disease ($n =?$). Imaging with hyperpolarized 3He was performed under an Institutional Review Board (IRB)-approved protocol with written informed consent obtained from each subject. In addition, all imaging was performed under a Food and Drug Administration approved physician's Investigational New Drug application (IND 57866) for hyperpolarized 3He. MRI data were acquired on a 1.5 T whole-body MRI scanner (Siemens Sonata, Siemens Medical Solutions, Malvern, PA) with broadband capabilities and a flexible 3He chest radiofrequency coil (RF; IGC Medical Advances, Milwaukee, WI; or Clinical MR Solutions, Brookfield, WI). During a 10–20-second breath-hold following the inhalation of $\approx$ 300 mL of hyperpolarized 3He mixed with $\approx$ 700 mL of nitrogen, a set of 19–28 contiguous axial sections were collected. Parameters of the fast low angle shot sequence for 3He MRI were as follows: repetition time msec / echo time msec, 7/3; flip angle, 10°; matrix, 80 $\times$ 128; field of view, 26 80 $\times$ 42 cm; section thickness, 10 mm; and intersection gap, none. The data were deidentified prior to analysis.

2.2 Algorithmic implementations

A fair and accurate comparison between algorithms necessitates several considerations which have been outlined previously (41). In designing the evaluation study:

- All algorithms and evaluation scripts have been implemented using open-source tools by the first author. The linear binning and hierarchical k-means algorithms were recreated using existing R functionality. These have been made available as part of the GitHub repository corresponding to this work.[2] Similarly, N4, Atropos-based lung segmentation, and the trained CNN approach are all available through ANTsR/ANTsRNet: `ANTsR::n4BiasFieldCorrection`, `ANTsR::functionalLungSegmentation`, and `ANTsRNet::elBicho`, respectively.[3] The weights for the CNN are publicly available and

[2] https://github.com/ntustison/Histograms

[3] Python versions are also available through ANTsPy/ANTsPyNet.

are automatically downloaded when running the program.

- The imaging data used for the evaluation is available upon request and through a data sharing agreement. All other data, including additional evaluation plots are available, in the specified GitHub repository.

2.3 Introduction of "El Bicho"

We extended the deep learning functionality first described in (38) to improve performance and provide a more clinically granular labeling (i.e., four clusters instead of two). In addition, further modifications incorporated additional data during training, added attention gating (42) to the U-net network (43) along with recommended hyperparameters (44), and a novel data augmentation strategy. More details are given below.

2.3.1 Network training

A 2-D U-net network was trained with several parameters recommended by recent U-net exploratory work (44). The images are sufficiently small such that 3-D training is possible. However, given the large voxel anisotropy for much of our data (both coronal and axial), we found a 2-D approach to be sufficient. Nevertheless, a 2.5-D approach is an optional way to run the code for isotropic data where network prediction can occur in more than one direction and the results averaged. Four total network layers were employed with 32 filters at the base layer which is doubled at each subsequent layer. Multiple training runs were performed where initial runs employed categorical cross entropy as the loss function. Upon convergence, training continued with a multi-label Dice loss function (45).

Training data (using an 80/20—training/testing split) was composed of the ventilation image, lung mask, and corresponding ventilation-based parcellation. The lung parcellation comprised four labels based on the Atropos-based ventilation-based segmentation (13). Six clusters were used to create the training data and combined to four for training. In using this GMM-MRF algorithm (which is the only one to use spatial information in the form of the MRF prior), we attempt to bootstrap a superior network-based segmentation approach by using the

(a) Original. (b) Nonlinear intensity warping. (c) Noise.

Figure 3: Custom data augmentation strategies for training to force a solution which focuses on the underlying ventilation-based lung structure. (b) Nonlinear intensity warping based on smoothly varying perturbations of the image histogram. (c) Additive Gaussian noise included for increasing the robustness of the segmentation network.

encoder-decoder structure of the U-net architecture as a dimensionality reduction technique. None of the evaluation data used in this work were used as training data. Responses from two subjects at the last layer of the network (with $n = 32$ filters) are given in Figure **??**

A total of five random slices per image were selected in the acquisition direction (both axial and coronal) for inclusion within a given batch (batch size = 128 slices). Prior to slice extraction, both random noise and randomly-generated, nonlinear intensity warping was added to the 3-D image (see Figure 3) using ANTsR/ANTsRNet functions (`ANTsR::addNoiseToImage`, and `ANTsRNet::histogramWarpImageIntensities`) with analogs in ANTsPy/ANTsPyNet . 3-D images were intensity normalized to have 0 mean and unit standard deviation. The noise model was additive Gaussian with 0 mean and a randomly chosen standard deviation value between [0, 0.3]. Histogram-based intensity warping used the default parameters. These data augmentation parameters were chosen to provide realistic but potentially difficult cases for training. In terms of hardware, all training was done on a DGX (GPUs: 4X Tesla V100, system memory: 256 GB LRDIMM DDR4).

2.3.2 Pipeline processing

An example R-based code snippet is provided in Listing 1 demonstrating how to process a single ventilation image using `ANTsRNet::elBicho`. If a simultaneous proton image has been

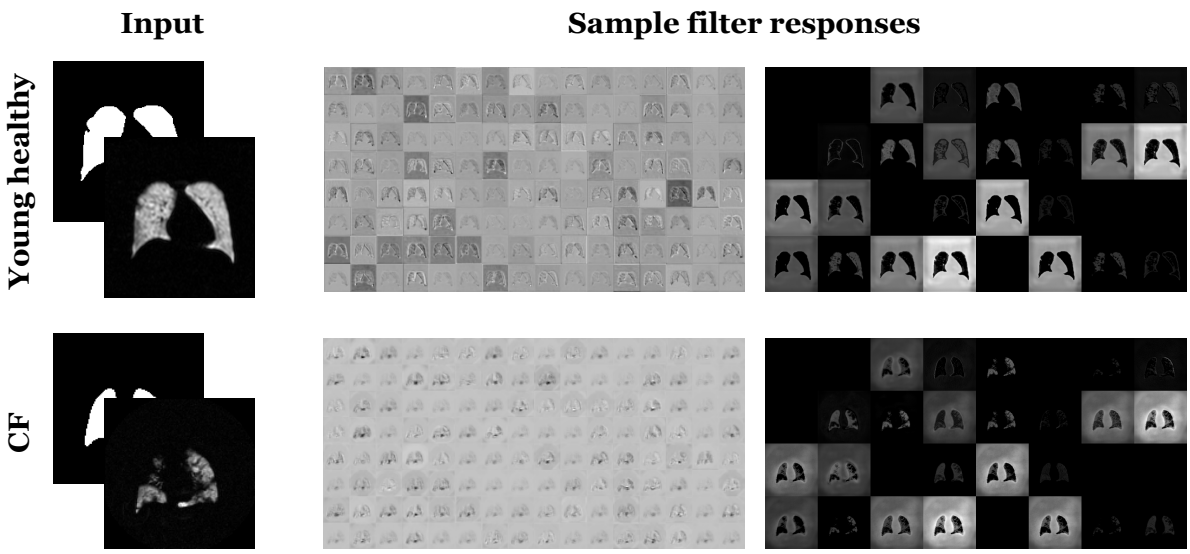

Figure 4: Optimized feature responses from the last layer of the U-net network generated from a (top) young healthy subject and (bottom) CF patient.

acquired, `ANTsRNet::lungExtraction` can be used to generate the requisite lung mask input. As mentioned previously, by default the prediction occurs slice-by-slice along the direction of anisotropy. Alternatively, prediction can be performed in all three canonical directions and averaged to produce the final solution.

```
library( ANTsR )
library( ANTsRNet )

# Read in proton and ventilation images.
protonImage <- antsImageRead( "proton.nii.gz" )
ventilationImage <- antsImageRead( "ventilation.nii.gz" )

# Use deep learning lung extraction to get lung mask from proton image.
lungMask <- lungExtraction( protonImage, modality = "proton", verbose = TRUE )

# Run deep learning ventilation-based segmentation.
seg <- elBicho( ventilationImage, lungMask, verbose = TRUE )

# Write segmentation and probability images to disk.
antsImageWrite( seg$segmentationImage, "segmentation.nii.gz" )
antsImageWrite( seg$probabilityImages[[1]], "probability1.nii.gz" )
antsImageWrite( seg$probabilityImages[[2]], "probability2.nii.gz" )
antsImageWrite( seg$probabilityImages[[3]], "probability3.nii.gz" )
antsImageWrite( seg$probabilityImages[[4]], "probability4.nii.gz" )
```

Listing 1: ANTsR/ANTsRNet command calls for processing a single ventilation image using ElBicho.

3 Results

Evaluations:

- Algorithmic precision
  - Three-tissue T1-weighted brain MRI segmentation (qualitative analog)
  - Input variance of reference distribution $\longrightarrow$ output variance (linear binning only)
  - Effects of simulated MR artefacts
- Algorithmic bias (in the absence of ground truth)
  - Dx prediction
  - STAPLE

3.1 Dx prediction

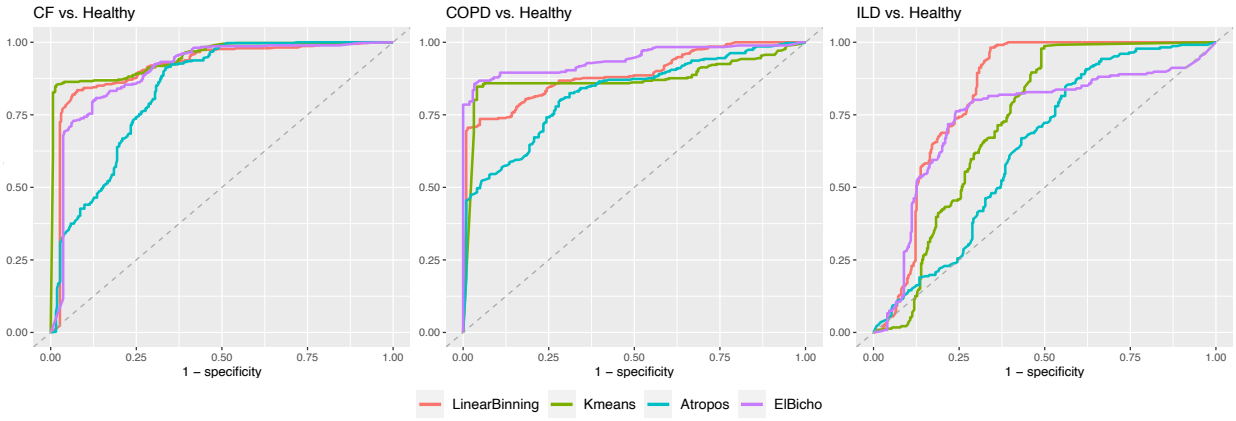

Figure 5

	CF vs. Healthy	COPD vs. Healthy	ILD vs. Healthy
Linear binning	0.92	0.89	0.83
Hier. k-means	0.95	0.87	0.73
Atropos	0.84	0.82	0.64
El Bicho	0.90	0.94	0.74

Table 1

In the absence of ground truth, this type of evaluation does confirm that these these measurements are clinically relevant. However, this is a very coarse assessment. For example, spirometry measures alone can be used to achieve highly accurate predictions using machine learning techniques (46).

3.2 T1-weighted brain segmentation analogy

As a preview of the

In Figure 6

Although the reference image set has been intensity normalized to $[0, 1]$ with truncated image intensities (quantiles $= [0, 0.99]$), it is apparent that the major features of the respective image histograms (specifically, the three peaks which correspond to the cerebrospinal fluid (CSF), gray matter (GM), and white matter (WM)) do not line up in this globally aligned space. Attempting to create a "reference" histogram from misaligned data is not without controversy. This can be seen in the results shown in the bottom where the linear binning analog drastically overstimates the amount of gray matter and simultaneously underestimates the amount of gray matter. The k-means approach, using precisely the same center clusters as determined via the reference histogram, yields a much better segmentation as it is optimizing the piecewise affine transform over histogram features. However, the hard threshold values result in labelings susceptible to noise in contrast to the GMM-MRF segmentation results.

3.3 Effect of reference image set selection

One important issue was whether or not to use the N4 bias correction algorithm as a preprocessing step. We ultimately decided to include it for a couple reasons. It is explicitly used in multiple algorithms (e.g., (8, 9, 13)) despite the issues raised previously and elsewhere (10) due to the fact that it qualitatively improves image appearance.[4]

There was another practical reason why this step was included and it concerns the reference

[4]This assessment is based on multiple conversations between the first author (as the developer of N4 and Atropos) and co-author Dr. Talissa Altes, one of the most experienced individuals in the field.

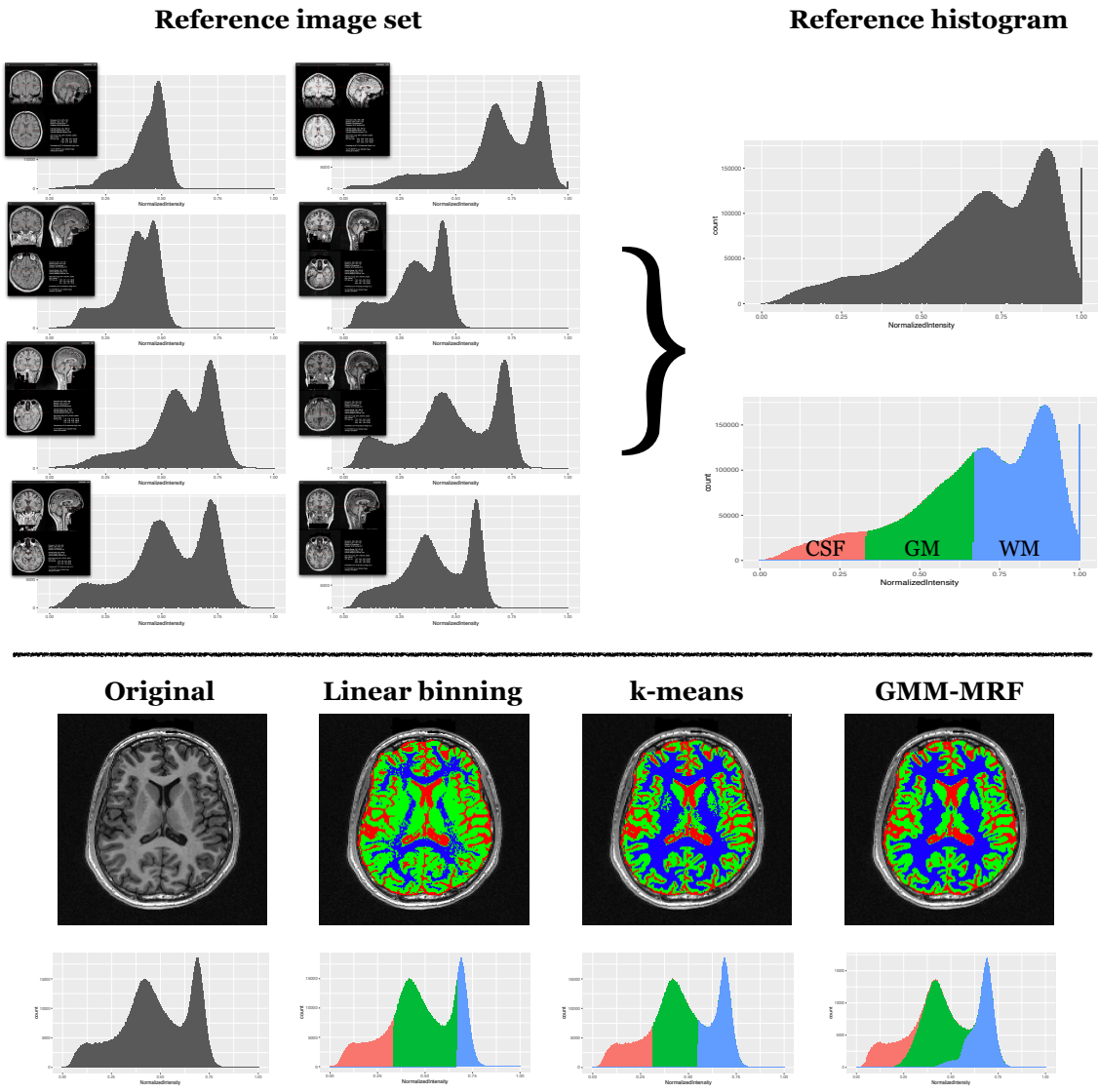

Figure 6: T1-weighted three-tissue brain segmentation analogy. Placing the three segmentation algorithms (i.e., linear binning, k-means, and GMM-MRF) in the context of brain tissue segmentation provides an alternative perspective for comparison. In the style of linear binning, we randomly select an image reference set using structurally normal individuals which is then used to create a reference histogram. (Bottom) For a subject to be processed, the resulting hard threshold values yield the linear binning segmentation solution as well as the initialization cluster values for both the k-means and GMM-MRF segmentations which are qualitatively different.

distribution required by the linear binning algorithm. As mentioned, a significant portion of N4 processing involves the deconvolution of the image histogram to sharpen the histogram peaks which decreases the standard deviation of the intensity distribution and can also

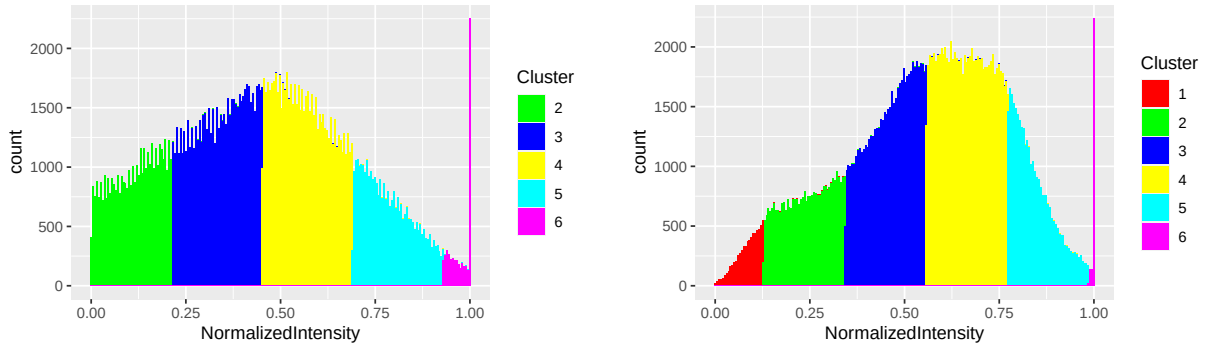

(a) Original: clustered reference distribution. (b) N4: clustered reference distribution.

Figure 7

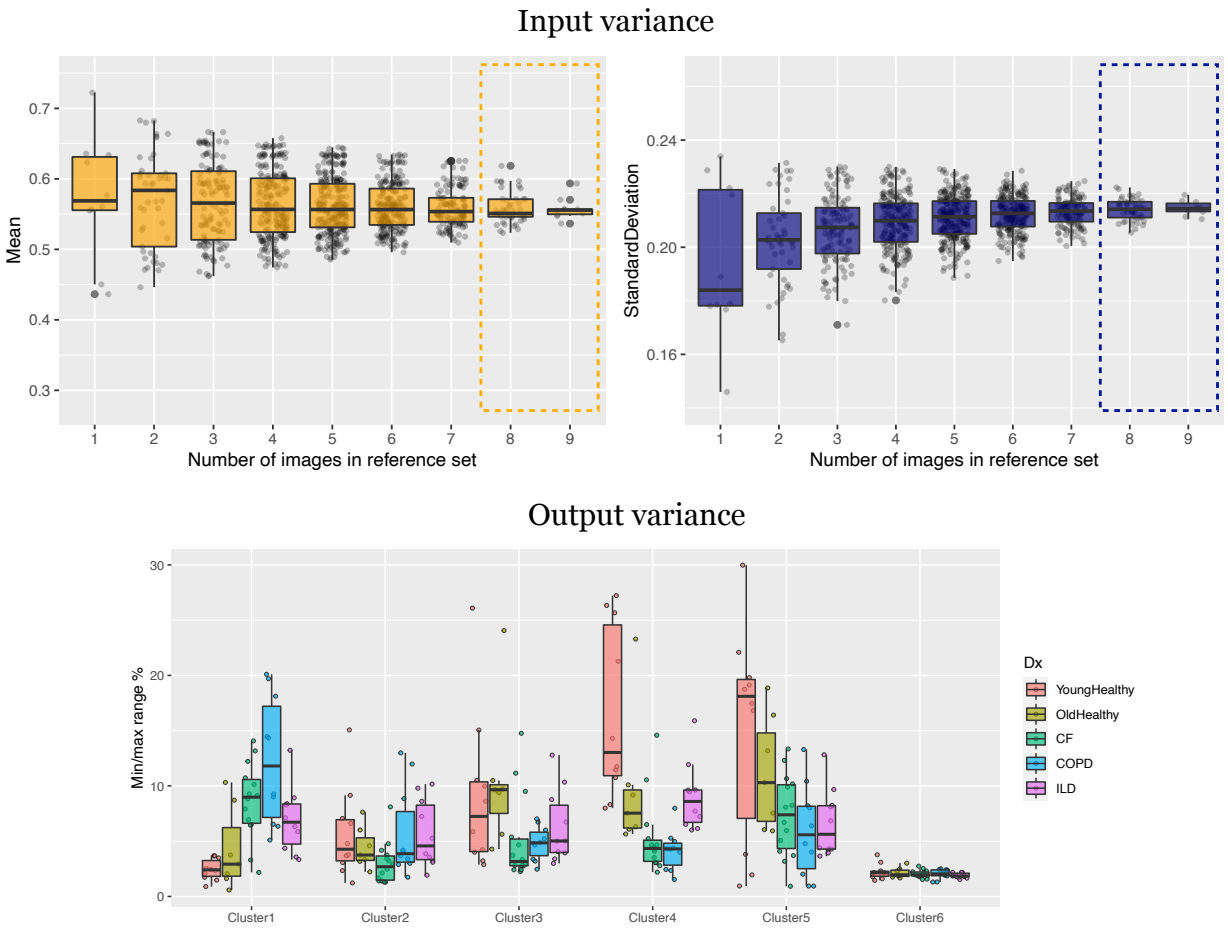

Figure 8

result in an histogram shift. Using the original set of 10 young healthy data with no N4 preprocessing, we created a reference distribution according to (9), which resulted in

		Noise	Nonlinearities	Noise and nonlinearities
Cluster 1	Linear binning	0.46 ± 0.34	0.71 ± 0.31	0.4 ± 0.32
	Hier. k-means	0.54 ± 0.28	0.77 ± 0.32	0.47 ± 0.3
	Atropos	0.92 ± 0.06	0.78 ± 0.2	0.78 ± 0.19
	El Bicho	0.89 ± 0.11	0.78 ± 0.26	0.73 ± 0.26
Cluster 2	Linear binning	0.73 ± 0.17	0.51 ± 0.27	0.5 ± 0.24
	Hier. k-means	0.67 ± 0.34	0.75 ± 0.28	0.54 ± 0.33
	Atropos	0.81 ± 0.13	0.46 ± 0.3	0.44 ± 0.27
	El Bicho	0.94 ± 0.04	0.73 ± 0.21	0.71 ± 0.21
Cluster 3	Linear binning	0.97 ± 0.04	0.89 ± 0.12	0.91 ± 0.09
	Hier. k-means	0.97 ± 0.05	0.95 ± 0.07	0.94 ± 0.08
	Atropos	0.98 ± 0.02	0.94 ± 0.06	0.93 ± 0.07
	El Bicho	0.98 ± 0.01	0.92 ± 0.08	0.91 ± 0.08
All clusters	Linear binning	0.89 ± 0.11	0.83 ± 0.15	0.81 ± 0.13
	Hier. k-means	0.94 ± 0.09	0.93 ± 0.1	0.9 ± 0.11
	Atropos	0.96 ± 0.04	0.87 ± 0.1	0.86 ± 0.1
	El Bicho	0.97 ± 0.02	0.87 ± 0.11	0.87 ± 0.11

Table 2

an approximate distribution of $\mathcal{N}(0.45, 0.24)$. This produced 0 voxels being classified as belonging to cluster 1 (i.e., ventilation defect) because two standard deviations from the mean is less than 0 and cluster 1 resides between -3 and -2 standard deviations. However using N4-preprocessed images produced something closer, $\mathcal{N}(0.56, 0.22)$, to the published values, $\mathcal{N}(0.52, 0.18)$, reported in (9), resulting in a non-empty set for cluster 1.

In addition to this pointing to a potential issue when applying linear binning to multi-site data, it prompted us to look at an associated precision issue due to reference cohort selection.

3.4 Effect of MR nonlinear intensity warping and additive noise

Need to add a SSIM calculation for each simulated image along with different histogram similarity measurements. We can then rescale all measurements for comparison and show how the SSIM calculation has lower variance than the histograms. THis shows that the image-to-histogram transformation results in information which is less robust than the original image.

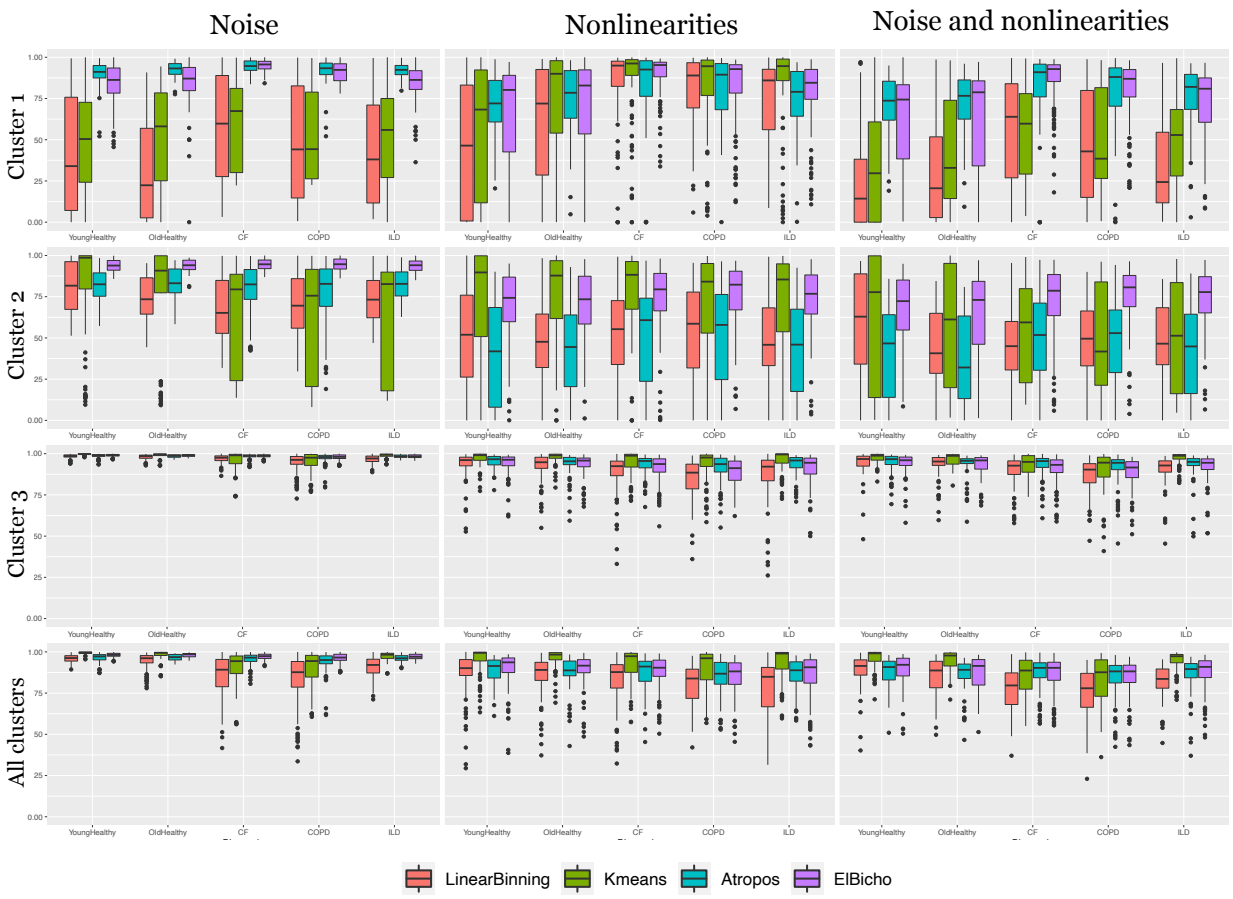

Figure 9

3.5 Diagnostic prediction

4 Discussion

Imagine, dear Reader, the reality of the future clinical application of functional lung imaging beyond mere research activity. In fact, imagine yourself being a patient on the receiving end of an imaging battery which includes hyperpolarized gas imaging. Now imagine that, upon receiving the images for assessment, the radiologist declares "Yes, these are nice but I'd rather work with the corresponding histograms." If this strikes you as absurd, then the point that we are trying to make should be clear.

We recognize that alternative deep learning strategies (hyperparameter choice, training data selection, etc.) could provide comparable and even superior performance to what was

presented. However, that is precisely our point—deep learning, generally, presents a much better alternative than histogram approaches as network training directly takes place in the image (i.e., spatial) domain and not in a transformed space where key information has been discarded.

As we mentioned previously, although susceptible to varyious levels of bias and lack of precision, these algorithms are decent for what they've been used for—global measurements, no more granular than spirometry, for doing research (while providing pretty visuals for publications.) However, if you want to do more sophisticated studies involving, for example, the spatial manifestation and/or growth of disease aided by advanced statistical techniques (such as similarity-driven multivariate linear reconstruction, then one should move beyond these shitty algorithms

In addition to the fundamental issues of precision and bias, we also point out that generally good modelling practice is to incorporate as much prior information as possible. Histogram-only algorithms throw out a significant portion of that prior information. This is a key consequence of the "No Free Lunch Theorem" (47)

Instead of investing time in propping up shitty algorithms, we should be donig things like looking at tailored network architectures/features and data augmentation strategies.

So, in summary:

- In addition to completely discarding spatial information, linear binning is based on overly simplistic assumptions, especially given common MR artefacts. The additional requirement of a reference distribution, with its questionable assumption of Gaussianity, is also a potential source of output variance.

- Hierarchical k-means also ignores spatial information and, although it does use a principled optimization criterion, this criterion is not adequately tailored for hyperpolarized gas imaging and relatively more susceptible to various levels of noise than competing approaches.

- The GMM-MRF approach does employ spatial considerations in the form of Markov random fields but these are highly simplistic prior modeling of local voxel neighborhoods which do not capture the complexity of ventilation defects/heterogeneity appearance in the images. Although the simplistic assumptions provide some robustness to noise, the highly variable histogram structure in the presence of MR nonlinearities causes significant variance in the resulting GMM fitting.

References

1. Bachert P, Schad LR, Bock M, et al.: Nuclear magnetic resonance imaging of airways in humans with use of hyperpolarized 3He. *Magn Reson Med* 1996; 36:192–6.

2. Kauczor HU, Hofmann D, Kreitner KF, et al.: Normal and abnormal pulmonary ventilation: Visualization at hyperpolarized He-3 MR imaging. *Radiology* 1996; 201:564–8.

3. Kauczor HU, Ebert M, Kreitner KF, et al.: Imaging of the lungs using 3He MRI: Preliminary clinical experience in 18 patients with and without lung disease. *J Magn Reson Imaging*; 7:538–43.

4. Altes TA, Powers PL, Knight-Scott J, et al.: Hyperpolarized 3He MR lung ventilation imaging in asthmatics: Preliminary findings. *J Magn Reson Imaging* 2001; 13:378–84.

5. Lange EE de, Mugler JP 3rd, Brookeman JR, et al.: Lung air spaces: MR imaging evaluation with hyperpolarized 3He gas. *Radiology* 1999; 210:851–7.

6. Samee S, Altes T, Powers P, et al.: Imaging the lungs in asthmatic patients by using hyperpolarized helium-3 magnetic resonance: Assessment of response to methacholine and exercise challenge. *J Allergy Clin Immunol* 2003; 111:1205–11.

7. Woodhouse N, Wild JM, Paley MNJ, et al.: Combined helium-3/proton magnetic resonance imaging measurement of ventilated lung volumes in smokers compared to never-smokers. *J Magn Reson Imaging* 2005; 21:365–9.

8. Shammi UA, D'Alessandro MF, Altes T, et al.: Comparison of hyperpolarized 3He and 129Xe MR imaging in cystic fibrosis patients. *Acad Radiol* 2021.

9. He M, Driehuys B, Que LG, Huang Y-CT: Using hyperpolarized 129Xe MRI to quantify the pulmonary ventilation distribution. *Acad Radiol* 2016; 23:1521–1531.

10. He M, Wang Z, Rankine L, et al.: Generalized linear binning to compare hyperpolarized 129Xe ventilation maps derived from 3D radial gas exchange versus dedicated multislice gradient echo mri. *Acad Radiol* 2020; 27:e193–e203.

11. Kirby M, Heydarian M, Svenningsen S, et al.: Hyperpolarized 3He magnetic resonance functional imaging semiautomated segmentation. *Acad Radiol* 2012; 19:141–52.

12. Kirby M, Svenningsen S, Owrangi A, et al.: Hyperpolarized 3He and 129Xe MR imaging in healthy volunteers and patients with chronic obstructive pulmonary disease. *Radiology* 2012; 265:600–10.

13. Tustison NJ, Avants BB, Flors L, et al.: Ventilation-based segmentation of the lungs using hyperpolarized (3)He MRI. *J Magn Reson Imaging* 2011; 34:831–41.

14. Thomen RP, Sheshadri A, Quirk JD, et al.: Regional ventilation changes in severe asthma after bronchial thermoplasty with (3)He MR imaging and CT. *Radiology* 2015; 274:250–9.

15. Gudbjartsson H, Patz S: The Rician distribution of noisy MRI data. *Magn Reson Med* 1995; 34:910–4.

16. Andersen AH: On the Rician distribution of noisy MRI data. *Magn Reson Med* 1996; 36:331–3.

17. Sled JG, Zijdenbos AP, Evans AC: A nonparametric method for automatic correction of intensity nonuniformity in MRI data. *IEEE Trans Med Imaging* 1998; 17:87–97.

18. Nyúl LG, Udupa JK: On standardizing the MR image intensity scale. *Magn Reson Med* 1999; 42:1072–81.

19. Wendt RE 3rd: Automatic adjustment of contrast and brightness of magnetic resonance images. *J Digit Imaging* 1994; 7:95–7.

20. Nyúl LG, Udupa JK, Zhang X: New variants of a method of MRI scale standardization. *IEEE Trans Med Imaging* 2000; 19:143–50.

21. Collewet G, Strzelecki M, Mariette F: Influence of MRI acquisition protocols and image intensity normalization methods on texture classification. *Magn Reson Imaging* 2004; 22:81–91.

22. De Nunzio G, Cataldo R, Carlà A: Robust intensity standardization in brain magnetic resonance images. *J Digit Imaging* 2015; 28:727–37.

23. Zhang Y, Brady M, Smith S: Segmentation of brain MR images through a hidden Markov random field model and the expectation-maximization algorithm. *IEEE Trans Med Imaging* 2001; 20:45–57.

24. Ashburner J, Friston KJ: Unified segmentation. *Neuroimage* 2005; 26:839–51.

25. Avants BB, Tustison NJ, Wu J, Cook PA, Gee JC: An open source multivariate framework for n-tissue segmentation with evaluation on public data. *Neuroinformatics* 2011; 9:381–400.

26. Cooley B, Acton S, Salemo M, et al.: Automated scoring of hyperpolarized helium-3 MR lung ventilation images: Initial development and validation. In *Proc intl soc mag reson med*; 2002.

27. Hartigan J, Wang M: A k-means clustering algorithm. *Applied Statistics* 1979; 28:100–108.

28. Vannier MW, Butterfield RL, Jordan D, Murphy WA, Levitt RG, Gado M: Multispectral analysis of magnetic resonance images. *Radiology* 1985; 154:221–4.

29. Besag J: On the statistical analysis of dirty pictures. *Journal of the Royal Statistical Society Series B (Methodological)* 1986; 48:259–302.

30. Dempster AP, Laird NM, Rubin DB: Maximum likelihood from incomplete data via the EM algorithm. *Journal of the Royal Statistical Society Series B (Methodological)* 1977; 39:1–38.

31. Tustison NJ, Avants BB, Cook PA, et al.: N4ITK: Improved N3 bias correction. *IEEE Trans Med Imaging* 2010; 29:1310–20.

32. Wang Z, Bovik AC, Sheikh HR, Simoncelli EP: Image quality assessment: From error visibility to structural similarity. *IEEE Trans Image Process* 2004; 13:600–12.

33. Svenningsen S, McIntosh M, Ouriadov A, et al.: Reproducibility of hyperpolarized 129Xe

MRI ventilation defect percent in severe asthma to evaluate clinical trial feasibility. *Acad Radiol* 2020.

34. Couch MJ, Thomen R, Kanhere N, et al.: A two-center analysis of hyperpolarized 129Xe lung MRI in stable pediatric cystic fibrosis: Potential as a biomarker for multi-site trials. *J Cyst Fibros* 2019; 18:728–733.

35. LeCun Y, Bengio Y, Hinton G: Deep learning. *Nature* 2015; 521:436–44.

36. Shen D, Wu G, Suk H-I: Deep learning in medical image analysis. *Annu Rev Biomed Eng* 2017; 19:221–248.

37. Zhang R, Isola P, Efros AA, Shechtman E, Wang O: The unreasonable effectiveness of deep features as a perceptual metric. In *2018 ieee/cvf conference on computer vision and pattern recognition*; 2018:586–595.

38. Tustison NJ, Avants BB, Lin Z, et al.: Convolutional neural networks with template-based data augmentation for functional lung image quantification. *Acad Radiol* 2019; 26:412–423.

39. Tustison NJ, Cook PA, Holbrook AJ, et al.: ANTsX: A dynamic ecosystem for quantitative biological and medical imaging. *medRxiv* 2021.

40. Warfield SK, Zou KH, Wells WM: Simultaneous truth and performance level estimation (STAPLE): An algorithm for the validation of image segmentation. *IEEE Trans Med Imaging* 2004; 23:903–21.

41. Tustison NJ, Johnson HJ, Rohlfing T, et al.: Instrumentation bias in the use and evaluation of scientific software: Recommendations for reproducible practices in the computational sciences. *Front Neurosci* 2013; 7:162.

42. Schlemper J, Oktay O, Schaap M, et al.: Attention gated networks: Learning to leverage salient regions in medical images. *Med Image Anal* 2019; 53:197–207.

43. Falk T, Mai D, Bensch R, et al.: U-net: Deep learning for cell counting, detection, and morphometry. *Nat Methods* 2019; 16:67–70.

44. Isensee F, Jaeger PF, Kohl SAA, Petersen J, Maier-Hein KH: nnU-Net: A self-configuring method for deep learning-based biomedical image segmentation. *Nat Methods* 2020.

45. Crum WR, Camara O, Hill DLG: Generalized overlap measures for evaluation and validation in medical image analysis. *IEEE Trans Med Imaging* 2006; 25:1451–61.

46. Badnjevic A, Gurbeta L, Custovic E: An expert diagnostic system to automatically identify asthma and chronic obstructive pulmonary disease in clinical settings. *Sci Rep* 2018; 8:11645.

47. Wolpert DH, Macready WG: No free lunch theorems for optimization. *Trans Evol Comp* 1997; 1:67–82.